

Rectifying Geometry-Induced Similarity Distortions for *Real-World* Aerial–Ground Person Re-Identification

Kailash A. Hambarde, Hugo Proen  a, *Senior Member, IEEE*

Abstract—Aerial–ground person re-identification (AG-ReID) is fundamentally challenged by extreme viewpoint and distance discrepancies between aerial and ground cameras, which induce severe geometric distortions and invalidate the assumption of a shared similarity space across views. The existing methods primarily use geometry-aware feature learning or appearance-conditioned prompting, and implicitly assume that the geometry-invariant dot-product similarity used within “attention” remains reliable under large viewpoint and distance variations. The main hypothesis in this work is that this assumption does not hold: extreme camera geometry and scale variations systematically distort the query–key similarity space, and heavily compromise attention-based matching, even when feature representations are partially aligned. To address this issue, we introduce the notion of *Geometry-Induced Query–Key Transformation* (GIQT), a lightweight and low-rank module that explicitly rectifies the similarity space by conditioning query–key interactions on camera geometry. Rather than modifying the feature content or the attention formulation itself, GIQT adapts the similarity computation to compensate for dominant, geometry-induced anisotropic distortions. Building on this local similarity rectification, we consider a geometry-conditioned prompt generation mechanism as an auxiliary component that provides global and view-adaptive representation priors, that are derived directly from camera geometry. Our experiments were carried out on four aerial-ground person re-identification benchmarks, and show that the proposed framework consistently improves the re-identification robustness under extreme and even previously unseen geometric perspectives. In practice, this work gives a step towards operation in high-altitude and large viewing-angle regimes. Also, such contribution is provided at minimal computational overheads, with respect to the state-of-the-art methods. <https://github.com/kailashhambarde/GeoReID.git>

I. INTRODUCTION

PERSON re-identification (ReID) is a classical problem of computer vision/machine learning domains, and aims to match identities across non-overlapping cameras [1]–[3]. Here, most significant progresses have been achieved in ground-to-ground ReID, using emerging network architectures and training strategies [6]–[8]. However, as ground-based camera networks remain limited in spatial coverage, efforts have been concentrated in using unmanned aerial vehicles (UAVs) to broaden surveillance capabilities [10], [11] of such type of systems. The combination of aerial and ground cameras gave rise to the aerial-ground person re-identification (AG-ReID)

Manuscript received February XX, 2025; revised XX XX, 2025.

This work was supported by national funds through FCT – Funda  o para a Ci  ncia e a Tecnologia, I.P., and, when applicable, co-funded by EU funds under project UID/50008/2025 – Instituto de Telecomunica  es.

Kailash A. Hambarde and Hugo Proen  a are with the Instituto de Telecomunica  es and the Department of Computer Science, Universidade da Beira Interior, Portugal.

Corresponding author: Kailash A. Hambarde (e-mail: kailash.hambarde@ubi.pt).

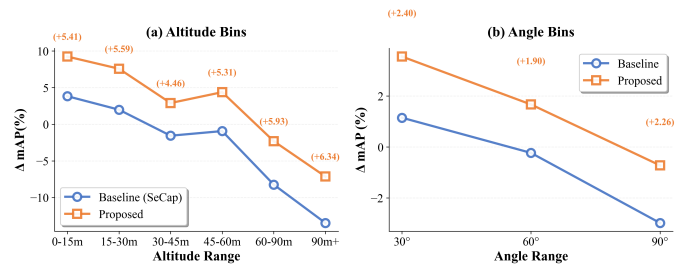


Fig. 1. Comparison between the performance degradation of the well known SeCap method as baseline and our proposal, across altitude and angle bins. The y-axis provide the $\Delta mAP = (\text{Bin mAP} - \text{Overall SeCap A} \rightarrow \text{G mAP})$. Values above zero indicate *better-than-overall* performance and values below zero indicate performance degradation. Overall, it is evident that the proposed method keeps superior performance in extreme geometric regimes.

problem, which requires to match identities across drastically different viewpoints and distances. AG-ReID is substantially more challenging than conventional ReID due to extreme perspective changes: aerial images often exhibit top-down or oblique views, while ground images typically capture frontal or profile appearances. Such viewpoint discrepancies induce severe geometric distortions, including scale compression, foreshortening, and body-part displacement, yielding large appearance variation and unreliable spatial correspondence across views [20], [21]. Beyond appearance variation, extreme camera geometry exposes a fundamental limitation of the existing ReID pipelines: the assumption of a shared similarity space across views. Modern transformer based ReID models rely on dot-product attention to compute similarity between local features [15], [51]. Even when feature representations are semantically aligned, viewpoint geometry warps spatial correspondence and feature orientation in a highly anisotropic manner [14], [27]. As a result, the geometry-invariant dot-product similarity used within attention becomes unreliable: corresponding regions may yield low similarity, while unrelated regions may spuriously align. Importantly, this does not indicate a limitation of attention or cross-attention mechanisms themselves, but rather a mismatch between extreme camera geometry and the default similarity metric used to compute attention weights. This behavior has been implicitly observed in prior AG-ReID studies, where performance degrades sharply as geometric disparity increases [25], [26]. This effect is empirically illustrated in Fig. 1, where performance degradation correlates monotonically with altitude and viewing-angle differences. The increasing performance gap under extreme geometry indicates that camera geometry introduces structured distortion in similarity computation rather than random noise. The existing AG-ReID methods mitigate cross-view disre-

ancies using attribute supervision [25], view-disentangled representations [27], or prompt-based feature adaptation. While effective in moderate settings, these approaches primarily rely on implicit learning of geometric relationships and typically ignore explicit camera geometry during similarity computation, limiting robustness under extreme or unseen viewpoints.

Motivated by these observations, we argue that robust AG-ReID requires explicitly accounting for geometry-induced distortion in cross-view similarity computation, rather than further modifying feature representations. To this end, we propose a geometry-conditioned similarity alignment framework that incorporates camera geometry into both global representation adaptation and local similarity computation.

The main contributions of this work are four-fold:

- We identify similarity-space distortion as a dominant failure mode in aerial–ground person re-identification under extreme camera geometry, showing that the geometry-invariant similarity assumption underlying attention becomes unreliable even when features are reasonably aligned.
- We propose a geometry-conditioned similarity alignment framework that explicitly adapts cross-view similarity computation rather than relying solely on feature adaptation.
- We introduce the Geometry-Induced Query–Key Transformation (GIQT), a lightweight and model-agnostic module that reshapes the attention similarity space via a geometry-conditioned low-rank transformation.
- We provide empirical evidence about a substantially stronger robustness and generalization under extreme and even unseen geometric conditions with respect to the state-of-the-art. Such improvements are observed across multiple AG-ReID benchmarks.

II. RELATED WORK

A. Aerial–Ground Person Re-Identification

Aerial-ground ReID extends conventional ReID to scenarios involving UAV-mounted and ground-based cameras, introducing extreme viewpoint, scale, and orientation discrepancies that fundamentally violate assumptions made in ground-to-ground settings [25], [33]. Unlike conventional ReID, where viewpoint variations are relatively limited, AG-ReID must cope with severe geometric distortions caused by altitude changes, oblique viewing angles, and drastic perspective shifts. Early research in AG-ReID primarily focused on benchmark construction to enable systematic evaluation. Nguyen et al. introduced the AG-ReID.v1 dataset [25] and its extension AG-ReID.v2 [26], highlighting the difficulty of matching identities across aerial and ground views. Zhang et al. proposed the large-scale synthetic CARGO benchmark to explicitly stress-test cross-view appearance changes under extreme geometry [27]. Subsequent video-based benchmarks, such as G2AVReID and AG-VPReID, incorporated temporal cues while retaining the same fundamental geometric challenges [34], [35]. These datasets demonstrate that appearance-driven representations are inherently fragile under extreme viewpoint geometry.

B. Implicit Geometry Modelling in AG-ReID

Most existing AG-ReID methods address viewpoint discrepancies through implicit feature learning. Multi-stream architectures separate aerial and ground representations and rely on auxiliary supervision, such as identity attributes, to encourage view-invariant encoding [26]. Transformer-based approaches, including the View-Decoupled Transformer (VDT), attempt to disentangle identity related and viewpoint related factors using view tokens and orthogonality constraints [27]. Prompt based methods, such as SeCap, further adapt representations through appearance conditioned prompts or dynamic token selection [31]. While effective in practice, these approaches learn geometric relationships implicitly from data. Viewpoint geometry such as camera altitude, viewing angle, or sensor configuration, is not explicitly modelled, limiting interpretability and control over how geometric distortions influence feature alignment. As a result, such methods often struggle to generalise under unseen or extreme viewpoint configurations.

C. Geometry Aware and View Invariant Learning

Several studies have explored mechanisms related to geometric robustness in cross view recognition. Adversarial domain adaptation has been employed to reduce distribution gaps between aerial and ground features [36], while view aware attention mechanisms attempt to capture view dependent transformations implicitly [27]. Diffusion based synthesis augments training data with generated cross view samples [37], and disentangled representation learning separates identity from view specific factors [26]. Rotation robustness has also been investigated through equivariant architectures and rotation-aware tokens [38]–[40]. However, these approaches primarily rely on data augmentation or implicit representation learning and do not explicitly incorporate known geometric priors. Crucially, readily available metadata in aerial sensing, such as altitude, viewing angle, and camera identity, are typically ignored during both representation learning and attention-based similarity computation.

D. Geometric Alignment and Multi-Modal Cues

Geometric and semantic alignment methods aim to reduce cross view mismatch by establishing correspondences across views. GSAlign leverages coupled geometric semantic alignment networks to learn dense correspondences [41], while part based and keypoint driven approaches rely on pose estimation to guide alignment [42], [43]. However, keypoint detection and part localization are unreliable in low resolution aerial imagery and under severe occlusion, limiting their effectiveness in AG-ReID scenarios. Multi modal approaches introduce textual or language-based supervision to enhance view invariance [44]–[46]. While promising, such methods increase system complexity and often depend on additional annotations or pretrained language models, making them less suitable for lightweight UAV-based deployment.

Despite significant progress, existing AG-ReID approaches share several limitations. First, geometric relationships are typically modeled implicitly, limiting interpretability and controllability. Second, robustness degrades substantially under

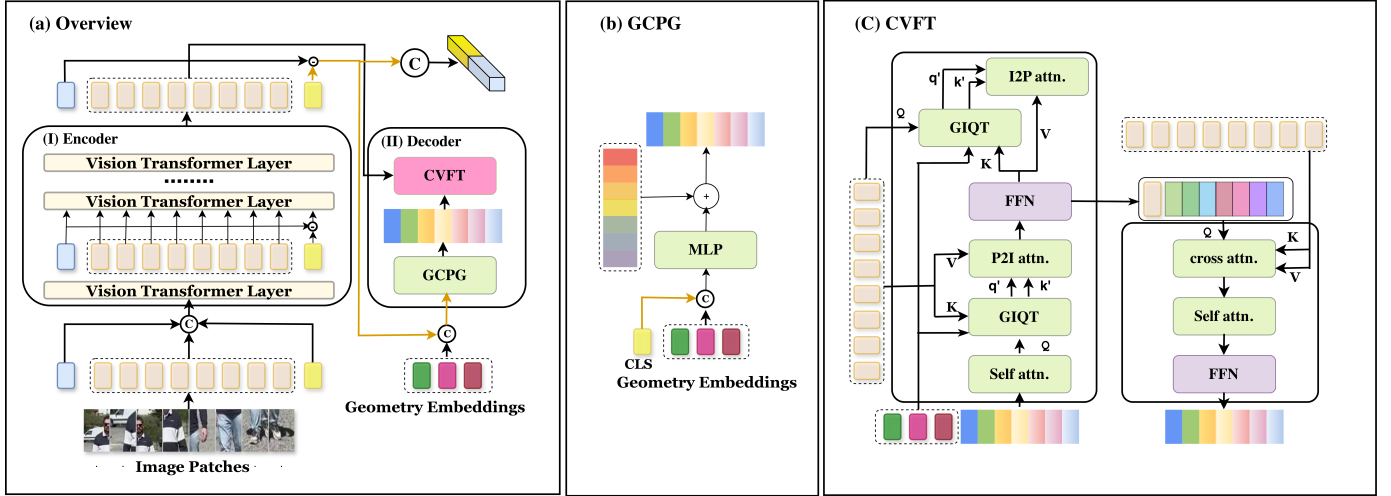


Fig. 2. Overview of the proposed geometry conditioned similarity alignment framework for aerial-ground person ReID. Camera geometry guides both global prompt adaptation and local similarity rectification via the proposed Geometry Induced Query Key Transformation (GIQT).

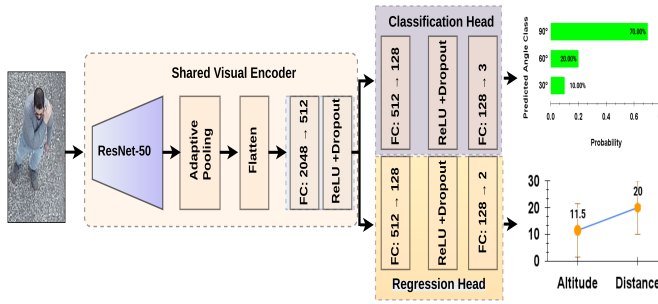


Fig. 3. Vision only multi task geometry prediction architecture. A shared ResNet-50 encoder extracts visual features from RGB images, followed by task specific heads for altitude and distance regression and viewing-angle classification.

extreme altitude and viewing-angle variations. Third, many methods introduce considerable computational overhead, hindering real-time UAV deployment. Finally, generalization across datasets with different camera geometries remains limited. These limitations motivate the need for explicitly geometry aware AG-ReID frameworks that directly incorporate aerial sensing priors into both global representation adaptation and local similarity computation, rather than relying solely on implicit feature learning.

III. METHOD

A. Overview

We propose a geometry conditioned similarity alignment framework for aerial-ground person ReID that explicitly incorporates camera geometry into both global representation adaptation and local similarity computation. An overview of the proposed framework is shown in Fig. 2. Given an input image X , a transformer based encoder $\mathcal{E}(\cdot)$ extracts a global identity token, a view related token, and a set of local patch features:

$$[\mathbf{z}_{\text{cls}}, \mathbf{z}_{\text{view}}, X_{\text{local}}] = \mathcal{E}(X). \quad (1)$$

Following view disentangled representation learning, we obtain a view invariant global descriptor by subtracting view related information from the global token:

$$X_{\text{inv}} = \mathbf{z}_{\text{cls}} - \mathbf{z}_{\text{view}}. \quad (2)$$

Rather than assuming a geometry invariant similarity space across views, our framework explicitly conditions cross view alignment on camera geometry. Geometry cues including altitude, viewing angle, and camera identity are encoded into a geometry embedding and used to modulate both global adaptation and local similarity computation. Specifically, the decoder integrates two complementary geometry aware mechanisms: a geometry conditioned prompt generator that provides global, view adaptive priors derived from camera geometry; and a Geometry Induced Query Key Transformation (GIQT) that adapts the similarity metric used within attention to compensate for viewpoint induced distortions during local feature matching.

The overall computation is summarized as:

$$\begin{aligned} X_{\text{inv}} &= \mathbf{z}_{\text{cls}} - \mathbf{z}_{\text{view}}, \\ P_{\text{geo}} &= \mathcal{G}_{\text{prompt}}(X_{\text{inv}}, \mathbf{e}_{\text{geo}}), \\ X_{\text{ref}} &= \mathcal{G}_{\text{align}}(X_{\text{local}}, P_{\text{geo}}, \mathbf{e}_{\text{geo}}), \\ \text{Out} &= [X_{\text{inv}}, X_{\text{ref}}]. \end{aligned} \quad (3)$$

where \mathbf{e}_{geo} denotes the geometry embedding. The proposed framework is model agnostic and can be instantiated using different encoder decoder architectures.

B. Geometry Metadata Acquisition

Our framework relies on camera geometry cues including altitude, horizontal distance, viewing angle, and camera identity. When such metadata is provided by the dataset, we directly encode the ground truth geometry. However, in many practical scenarios, geometry metadata may be unavailable or incomplete. To address this, we train a vision only multi task geometry prediction network to estimate geometry cues directly from RGB images. As shown in Fig. 3, a shared

ResNet-50 encoder extracts visual features, followed by task specific heads for altitude and distance regression and viewing angle classification. The predicted geometry is used consistently during both training and inference, enabling geometry conditioned alignment without requiring external sensors or metadata.

C. Geometry Conditioned Prompt Generation

Global cross view alignment requires adapting high level representation priors to camera geometry. To this end, we introduce a geometry conditioned prompt generation module that maps camera geometry directly to global prompt offsets.

$$\mathbf{e}_{\text{geo}} = [\mathbf{e}_{\text{alt}}; \mathbf{e}_{\text{angle}}; \mathbf{e}_{\text{cam}}]. \quad (4)$$

Given the view invariant descriptor X_{inv} and geometry embedding \mathbf{e}_{geo} , geometry conditioned prompts are generated as:

$$P_{\text{geo}} = P_{\text{base}} + \alpha \cdot f_{\text{geo}}(X_{\text{inv}}, \mathbf{e}_{\text{geo}}). \quad (5)$$

The residual formulation preserves identity discriminative semantics while injecting geometry as a structured bias, enabling controlled adaptation with minimal overhead. Geometry conditioned prompts act as global priors that guide the decoder toward geometry consistent cues under varying viewpoints.

D. Geometry Induced Query Key Transformation

While geometry conditioned prompts provide coarse global adaptation, extreme viewpoint changes introduce local geometric distortions that challenge the geometry invariant similarity assumption used within attention. The proposed Geometry Induced Query Key Transformation explicitly addresses this issue by adapting the similarity metric used to compute attention weights. Empirical analysis of cross view feature covariance reveals pronounced spectral decay, indicating that viewpoint induced distortions are highly anisotropic. A small number of dominant components capture most geometry induced variation, motivating a low rank correction strategy. Before computing attention, geometry conditioned transformations are applied to queries and keys:

$$Q' = T_Q(\mathbf{e}_{\text{geo}})Q, \quad K' = T_K(\mathbf{e}_{\text{geo}})K. \quad (6)$$

Values are kept unchanged to preserve feature content, while the similarity computation is adapted to viewpoint geometry. To avoid over parameterization, we adopt a low rank residual formulation:

$$T(\mathbf{e}_{\text{geo}}) = I + U(\mathbf{e}_{\text{geo}})V(\mathbf{e}_{\text{geo}})^\top. \quad (7)$$

By adapting the comparison space rather than feature content, GIQT suppresses unstable viewpoint dependent similarity directions and emphasizes geometry consistent cues, enabling robust local alignment beyond what prompt adaptation alone can achieve.

E. Geometry Aligned Local Feature Refinement

Local features are refined through a geometry aligned two way attention mechanism that integrates geometry conditioned prompts and GIQT.

$$\begin{aligned} F_{\text{P}} &= \text{FFN}(\text{CA}(\text{SA}(P_{\text{geo}}), X_{\text{local}}, X_{\text{local}})) + P_{\text{geo}}, \\ F_{\text{I}} &= \text{CA}(X_{\text{local}}, F_{\text{P}}, F_{\text{P}}) + X_{\text{local}}. \end{aligned} \quad (8)$$

$$[\mathbf{Out}, *] = \text{FFN}(\text{SA}(\text{CA}([\mathbf{Out}, F_{\text{P}}], F_{\text{I}}, F_{\text{I}}))). \quad (9)$$

The resulting refined features are explicitly aligned with respect to camera geometry, yielding robust local representations under extreme cross-view variations.

F. Optimization

We apply identity classification and triplet losses to both global and refined local features. View disentanglement is regularized using view classification and orthogonality constraints:

$$\mathcal{L}_{\text{view}} = - \sum_i y_i \log p_i, \quad \mathcal{L}_{\text{orth}} = \sum_{i=1}^d |\langle \mathbf{inv}_i, \mathbf{v}_i \rangle|. \quad (10)$$

To stabilize geometry conditioned prompt adaptation, an ℓ_2 regularization term is applied to the prompt offset. The final training objective is:

$$\begin{aligned} \mathcal{L} &= \alpha(\mathcal{L}_{\text{ID}}^{\text{global}} + \mathcal{L}_{\text{Tri}}^{\text{global}}) + \beta(\mathcal{L}_{\text{ID}}^{\text{local}} + \mathcal{L}_{\text{Tri}}^{\text{local}}) \\ &\quad + \lambda(\mathcal{L}_{\text{view}} + \mathcal{L}_{\text{orth}}) + \gamma \mathcal{L}_{\text{geo}}. \end{aligned} \quad (11)$$

We set $(\alpha, \beta, \lambda, \gamma) = (1.0, 1.0, 0.5, 0.1)$ in all experiments.

G. Vision Based Geometry Metadata Prediction

Our framework conditions similarity alignment on camera geometry cues, including altitude, horizontal distance, viewing angle, and camera identity. When such metadata is provided by the dataset, we directly use the ground-truth geometry. To enable geometry conditioned alignment when metadata is unavailable or incomplete, we employ a vision only multi-task geometry prediction network shown in Fig. 3. The network consists of a shared ResNet-50 encoder followed by task specific heads that perform altitude and distance regression and viewing-angle classification. The predicted geometry is used to construct the geometry embedding \mathbf{e}_{geo} and is applied consistently during both training and inference. When ground truth geometry is available, the predictor is not used.

IV. EXPERIMENTS

A. Datasets and Evaluation Protocols

Datasets. We evaluate our approach on four aerial-ground person ReID benchmarks: AG-ReIDv1 [25], AG-ReIDv2 [26], CARGO [27], and DetReIDX [28]. AG-ReIDv1 and AG-ReIDv2 provide ground truth camera geometry annotations, including drone altitude and camera identity. DetReIDX provides drone altitude, viewing angles, and camera identity. In contrast, CARGO only provides camera identity and does not include explicit geometric metadata such as altitude or

viewing angle. The CARGO dataset contains 108,563 images of 5,000 identities captured by eight ground cameras and five aerial cameras. AG-ReIDv1 consists of 21,983 images of 388 identities collected using one aerial camera and one ground camera, with aerial views captured at altitudes ranging from 15 to 45 meters. AG-ReIDv2 extends AG-ReIDv1 by introducing additional viewpoints, more identities, and more diverse camera configurations. DetReIDX contains 553 identities and includes one training split and three evaluation protocols: $A \rightarrow A$ (105,478 images), $A \rightarrow G$ (72,033 images), and $G \rightarrow A$ (72,033 images). The dataset is collected across six international university campuses and features substantial variation in drone altitude and viewing angle. For CARGO, we use the proposed vision-only geometry predictor to generate altitude, horizontal distance, and viewing angle. For AG-ReIDv1 and AG-ReIDv2, the geometry predictor is used only to estimate viewing angles when ground-truth angle annotations are unavailable.

Evaluation Protocols. Following common practice in aerial-ground person ReIDs we evaluate all methods using the Cumulative Matching Characteristic (CMC) at Rank-1 [64] and mean Average Precision (mAP) [65]. For the CARGO dataset, we follow the benchmark defined protocols and report results under four settings: *ALL*, which evaluates performance across all query-gallery pairs; $G \leftrightarrow G$, which evaluates ground-to-ground matching; $A \leftrightarrow A$, which evaluates aerial-to-aerial matching; and $A \leftrightarrow G$, which evaluates the most challenging aerial-to-ground matching scenario. For AG-ReIDv1, we adopt the standard bidirectional cross view evaluation protocol between aerial and ground cameras, namely $A \rightarrow G$ and $G \rightarrow A$. AG-ReIDv2 extends AG-ReIDv1 by introducing additional camera viewpoints. In particular, the wearable view (W) represents a low viewpoint close to human eye level, while the ground view (G) corresponds to fixed CCTV-style cameras. Based on these views, AG-ReIDv2 defines four cross view protocols: $A \rightarrow G$, $G \rightarrow A$, $A \rightarrow W$, and $W \rightarrow A$. For DetReIDX, we follow the official evaluation protocol and report results under three settings: $A \rightarrow A$, $A \rightarrow G$, and $G \rightarrow A$. These protocols involve significant variation in drone altitude, viewing angle, and image resolution, making cross-view retrieval particularly challenging. In all cases, A denotes aerial views, G denotes ground views, and W denotes wearable views. The arrow indicates the retrieval direction from query to gallery, while the double arrow indicates bidirectional evaluation. All methods are evaluated using identical train test splits and metrics to ensure fair and reproducible comparison.

B. Implementation Details

Our proposed method is implemented using PyTorch and the FastReID framework. All experiments are conducted on NVIDIA A40 GPUs. We adopt a pre-trained Vision Transformer Base (ViT-B/16) as the backbone network, initialized with ImageNet pre-trained weights. All input images are resized to $256 \times 128 \times 3$ pixels. For data augmentation, we apply random horizontal flipping, padding, and random erasing [67] with a probability of 0.5. The model is trained using a mini-batch size of 128 (or 192 for larger datasets),

TABLE I
PERFORMANCE COMPARISON ON AG-REID UNDER TWO CROSS-VIEW PROTOCOLS. ALL METHODS ARE EVALUATED UNDER IDENTICAL TRAINING AND TESTING SETTINGS. METHODS NOT ORIGINALLY DESIGNED FOR AG-REID ARE ADAPTED FOLLOWING THEIR OFFICIAL IMPLEMENTATIONS. GEOMETRY INFORMATION IS PROVIDED ONLY TO METHODS THAT EXPLICITLY SUPPORT GEOMETRY CONDITIONING. BEST RESULTS ARE HIGHLIGHTED AS **BOLD**, AND SECOND-BEST RESULTS ARE HIGHLIGHTED AS UNDERLINE.

Method	Protocol 1: $A \leftrightarrow G$		Protocol 2: $G \leftrightarrow A$	
	Rank1	mAP	Rank1	mAP
SBS [47]	73.54	59.77	73.70	62.27
BoT [48]	70.01	55.47	71.20	58.83
OsNet [49]	72.59	58.32	74.22	60.99
VV [50]	77.22	67.23	79.73	69.83
Explain [55]	81.28	72.38	82.64	73.35
VIT [51]	81.47	72.61	82.85	73.39
TrasReID [15]	81.80	73.10	83.40	74.60
PFD [59]	82.30	73.60	82.50	73.90
PHA [18]	79.30	71.30	81.10	72.10
FusionReID [56]	80.40	71.40	82.40	74.20
PCL-CLIP [57]	82.16	73.11	86.90	76.28
DTST [43]	83.48	74.51	84.72	76.05
VDT [27]	82.91	74.44	86.59	78.57
CLIP-ReID [19]	72.61	62.09	74.12	64.19
AG-ReID [25]	82.91	72.38	82.85	73.35
SeCap [31]	84.03	76.16	87.01	78.34
LATex [45]	85.26	77.67	<u>89.40</u>	81.15
SD-ReID [37]	85.16	75.40	77.02	<u>85.57</u>
GSAAlign [41]	86.74	84.00	87.94	87.17
GeoReID	87.02	79.46	90.64	83.55

where each batch consists of 32 identities with 4 instances per identity (or 8 instances for datasets with more samples per identity). The model is optimized using SGD [66] with a base learning rate of 0.008 for 120 epochs on the dataset size. We employ a cosine annealing learning rate schedule with a minimum learning rate of 1.6×10^{-6} and a warmup period of 2000 iterations. The weight decay is set to 0.0001, and gradient clipping is enabled for training stability. Mixed precision training (Automatic Mixed Precision) is utilized to accelerate training and reduce memory consumption.

C. Comparison with State-of-the-art Methods

We evaluate the proposed GeoReID framework on four aerial-ground person ReID benchmarks, namely AG-ReIDv1, AG-ReIDv2, CARGO, and DETReIDX, and compare it with a wide range of state-of-the-art methods. Quantitative results on AG-ReID are reported in Table I. GeoReID achieves the highest Rank-1 accuracy under both $A \leftrightarrow G$ and $G \leftrightarrow A$ evaluation protocols. Under the $A \leftrightarrow G$ setting, GeoReID attains 87.02% Rank-1 accuracy and 79.46% mAP, improving upon the strongest prior Rank-1 result while maintaining competitive retrieval quality. Under the $G \leftrightarrow A$ setting, GeoReID further achieves 90.64% Rank-1 accuracy and 83.55% mAP, surpassing previous methods in Rank-1 performance. These results indicate that geometry conditioned similarity alignment consistently improves cross view matching accuracy. Results on AG-ReIDv2 are summarized in Table II, which reports performance across four cross view protocols ($A \rightarrow G$, $G \rightarrow A$, $A \rightarrow W$, and $W \rightarrow A$). GeoReID achieves the best overall performance across all protocols. Under the most challenging $A \rightarrow G$ setting, GeoReID reaches 91.26% Rank-1 accuracy and

TABLE II

PERFORMANCE COMPARISON ON THE AG-ReIDv2 DATASET ACROSS FOUR PROTOCOLS. BEST RESULTS ARE HIGHLIGHTED AS **BOLD**, AND SECOND-BEST RESULTS ARE HIGHLIGHTED AS UNDERLINED.

Model	A→G		G→A		A→W		W→A	
	Rank1 mAP							
Swin [32]	68.76	57.66	68.80	57.70	68.49	56.15	64.40	53.90
HRNet-18 [52]	75.21	65.07	76.25	66.16	76.26	66.17	76.25	66.17
SwinV2 [53]	76.44	66.09	77.11	62.14	80.08	69.09	74.53	65.61
MGN (R50) [54]	82.09	70.17	84.21	72.41	88.14	78.66	84.06	73.73
BoT (R50) [48]	80.73	71.49	79.46	69.67	86.06	75.98	82.69	72.41
SBS (R50) [47]	81.43	72.19	80.15	70.37	86.66	76.68	83.29	73.11
ViT [51]	85.40	77.03	84.65	75.90	89.77	80.48	84.27	76.59
TransReID [15]	88.00	81.40	87.60	80.10	90.40	84.50	87.70	81.10
FusionReID [56]	86.70	80.70	87.90	80.00	89.70	84.20	86.50	80.90
CLIP-ReID [19]	85.36	79.79	85.64	79.08	89.14	84.23	86.50	79.55
PCL-CLIP [57]	79.80	72.20	81.12	72.40	87.14	77.70	84.19	73.89
V2E AGREIDv2 [26]	88.77	80.72	87.86	78.51	93.62	84.85	88.61	80.11
Explain [55]	87.70	79.00	87.35	78.24	93.67	83.14	87.73	79.08
VDT [27]	86.46	79.13	86.14	78.12	90.00	82.21	85.26	78.52
SeCap [31]	88.12	80.84	88.24	79.99	91.44	84.01	87.56	80.15
SD-ReID [37]	87.04	80.61	86.74	79.24	90.86	84.06	87.86	81.01
LATex [45]	89.13	83.50	89.01	82.85	91.35	86.35	89.32	83.30
GeoReID	91.26	85.52	90.34	83.88	93.21	88.03	90.95	84.79

85.52% mAP, outperforming all competing methods. Consistent improvements are also observed under G→A, where GeoReID achieves 90.34% Rank-1 accuracy and 83.88% mAP. Notably, GeoReID yields strong gains under the A→W and W→A protocols, which involve low elevation wearable viewpoints and severe viewpoint asymmetry, achieving the highest mAP in both cases. These results demonstrate that rectifying geometry induced distortion in the similarity space leads to more reliable cross view ranking under heterogeneous camera configurations.

Quantitative results on the CARGO dataset are reported in Table III. CARGO represents a realistic metadata free aerial-ground ReID scenario, where camera geometry annotations are unavailable and must be estimated. GeoReID achieves the best overall performance under the All protocol, with 71.79% Rank-1 accuracy and 63.69% mAP. Under the most challenging A→G protocol, GeoReID attains 72.02% Rank-1 accuracy and 64.61% mAP, outperforming all competing methods. This setting involves the largest viewpoint, scale, and perspective discrepancies, highlighting the effectiveness of geometry conditioned similarity rectification for difficult cross-view matching. Performance on same view protocols (G→G and A→A) remains competitive, indicating that geometry conditioning does not compromise same view discrimination. These results show that GeoReID remains effective even when camera geometry is predicted rather than provided. Results on the DETReIDX dataset are summarized in Table IV. DETReIDX is particularly challenging due to noisy detections, low image resolution, and extreme aerial-ground viewpoint differences, leading to low absolute performance across all methods. GeoReID achieves the best performance under the A→G protocol, obtaining 20.84% Rank-1 accuracy and 23.13% mAP. Across all three evaluation protocols, Geo-

TABLE III

PERFORMANCE COMPARISON ON THE CARGO DATASET UNDER METADATA-FREE SETTINGS. THE CARGO DATASET DOES NOT PROVIDE CAMERA GEOMETRY ANNOTATIONS. WE GENERATE ALTITUDE, HORIZONTAL DISTANCE, AND VIEWING ANGLE USING OUR VISION-ONLY META PREDICTOR. THE SAME PREDICTED GEOMETRY IS PROVIDED TO ALL GEOMETRY-AWARE BASELINES, WHILE METHODS WITHOUT GEOMETRY MODELING ARE EVALUATED WITHOUT GEOMETRY INFORMATION. BEST RESULTS ARE HIGHLIGHTED AS **BOLD**, AND SECOND-BEST RESULTS ARE HIGHLIGHTED AS UNDERLINED.

Model	All		G→G		A→A		A→G	
	Rank-1 mAP							
SBS [47]	50.32	43.09	72.31	62.99	67.50	49.73	31.25	29.00
PCB [63]	51.00	44.50	74.10	67.60	55.00	44.60	34.40	30.40
BoT [48]	54.81	46.49	77.68	66.47	65.00	49.79	36.25	32.56
MGN [54]	54.81	49.08	83.93	71.05	65.00	52.96	31.87	33.47
VV [50]	45.83	38.84	72.31	62.99	67.50	49.73	31.25	29.00
AGW [60]	60.26	53.44	81.25	71.66	67.50	56.48	43.57	40.90
BAU [61]	45.20	38.40	61.60	51.20	50.00	42.60	40.40	36.70
PAT [62]	37.90	15.30	52.70	24.20	50.00	23.10	35.10	15.50
DTST [43]	64.42	55.73	78.57	72.40	80.00	63.31	50.53	43.49
ViT [51]	61.54	53.54	82.14	71.34	80.00	64.47	43.13	40.11
VDT [27]	64.10	55.20	82.14	71.59	82.50	66.83	48.12	42.76
TransReID [15]	73.70	<u>64.70</u>	85.70	77.90	85.00	71.80	64.40	55.90
FusionReID [56]	67.90	61.50	85.70	79.40	80.00	<u>69.30</u>	48.30	53.10
CLIP-ReID [19]	68.27	64.25	84.82	<u>80.80</u>	75.00	65.42	55.62	53.83
PCL-CLIP [57]	67.31	60.93	84.82	76.00	70.00	60.75	54.43	51.43
SD-ReID [37]	<u>70.48</u>	61.42	81.25	74.08	82.50	67.70	48.75	46.37
GSALIGN [41]	65.06	57.95	83.04	73.86	80.00	65.55	64.89	<u>61.55</u>
SeCap [31]	68.59	60.19	<u>86.61</u>	75.42	80.00	68.08	<u>69.43</u>	58.94
GeoReID	71.79	63.69	88.04	79.14	<u>82.51</u>	68.20	72.02	64.61

TABLE IV

PERFORMANCE COMPARISON ON THE DETREIDX DATASET ACROSS THREE EVALUATION PROTOCOLS. RESULTS ARE REPORTED USING THE BEST VALIDATION CHECKPOINT. BEST VALUES PER COLUMN ARE SHOWN IN **BOLD**.

Method	G→A		A→G		A→A	
	Rank-1 mAP					
SBS [47]	46.74	13.53	15.59	15.51	13.74	9.09
MGN [54]	46.48	14.62	15.10	16.33	13.06	8.97
AGW [60]	30.59	8.56	12.30	13.13	10.85	6.84
VDT [27]	50.36	<u>16.37</u>	<u>18.14</u>	<u>18.55</u>	<u>15.27</u>	<u>9.35</u>
SeCap [31]	51.63	14.86	17.05	17.77	14.03	9.12
GeoReID	48.87	21.28	20.84	23.13	16.28	12.97

ReID consistently achieves the highest mAP, indicating more reliable ranking quality under severe geometric distortion. Under the G→A setting, GeoReID attains the highest mAP despite slightly lower Rank-1 accuracy, while performance on the A→A protocol also improves consistently. These results confirm that explicitly rectifying geometry induced similarity distortion is particularly beneficial in extremely challenging cross view scenarios.

D. Ablation Studies and Analysis

Component Ablation Analysis

This section analyzes the contribution of each proposed component and geometry cue across four benchmarks with progressively increasing geometric difficulty: AG-ReID, AG-ReIDv2, CARGO, and DETReIDX.

1) *Component Level Analysis*: We first evaluate the individual and combined effects of geometry conditioned prompts and the GIQT. As shown in Table VI, adding GCPG improves Rank-1 accuracy from 84.03% to 86.46%, confirming that

TABLE V
ABLATION AND GEOMETRY EMBEDDING ANALYSIS ON DETREIDX

Method	G→A		A→G		A→A	
	R1	mAP	R1	mAP	R1	mAP
+ GCPG	46.33	19.47	19.13	21.30	13.73	11.74
+ GIQT	46.59	19.82	19.63	22.04	15.30	12.14
+ GCPG + GIQT	47.42	20.32	20.06	22.76	15.85	12.09
<i>Geometry Embedding Analysis</i>						
w/o Cam	46.57	19.38	18.46	21.04	14.19	11.93
w/o Alt	47.51	20.36	20.11	22.56	14.81	11.77
w/o Ang	47.31	20.15	20.22	22.54	14.94	12.06

TABLE VI
ABLATION STUDY ON AG-ReID

Method	A↔G		G↔A	
	R1	mAP	R1	mAP
Baseline (SeCap)	84.03	76.20	87.21	79.19
+ GCPG	86.46	78.68	89.50	82.24
+ GIQT	85.47	77.36	87.97	79.73
+ GCPG + GIQT	87.02	79.46	90.64	83.55
<i>Geometry Embedding Analysis</i>				
w/o Cam	86.37	79.39	89.50	82.61
w/o Alt	84.50	75.99	86.38	78.77
w/o Ang	86.37	78.83	88.88	81.52

global representation priors benefit from explicit geometry conditioning. GIQT alone provides smaller but consistent gains, indicating the presence of local similarity distortion even when global features are unchanged. Combining GCPG and GIQT yields the best results across both A↔G and G↔A protocols, demonstrating complementary effects between global adaptation and local similarity rectification. Table VII shows that the same trend holds under more diverse camera configurations, including wearable views. GCPG provides strong improvements across all protocols, while GIQT yields consistent gains, particularly in cross view settings. The combined GCPG+GIQT model achieves the best overall performance, with notable improvements under the challenging A↔G and W↔A protocols, where viewpoint asymmetry is most severe. CARGO represents a metadata free scenario where geometry must be predicted. As shown in Table VIII, GIQT yields larger gains than GCPG under the most challenging A→G protocol, improving Rank-1 accuracy from 71.28% to 72.34%. This suggests that under extreme cross view mismatch and imperfect geometry estimation, correcting similarity space distortion becomes more critical than global prompt adaptation alone. DETReIDX is characterised by noisy detections, low resolution, and extreme aerial-ground viewpoint differences. As shown in Table V, GCPG and GIQT individually provide modest gains, while their combination achieves the highest mAP across all protocols. Although absolute performance remains low due to dataset difficulty, the consistent improvement in mAP indicates more reliable ranking under severe geometric distortion.

Geometry Embedding Analysis

We further analyze (Table V, VI, VII, VIII) the contribution of individual geometry cues by removing camera identity, altitude, and viewing-angle encoding. Across all datasets, removing altitude or viewing angle information leads to larger performance degradation than removing camera identity. For example, on AG-ReID (Table VI), removing altitude reduces

TABLE VII
ABLATION STUDY ON AG-ReIDv2

Method	A↔G		G↔A		A↔W		W↔A	
	R1	mAP	R1	mAP	R1	mAP	R1	mAP
Baseline (SeCap)	88.12	80.84	88.24	79.99	91.44	84.01	87.56	80.15
+ GCPG	90.24	84.41	88.90	83.45	93.30	87.65	90.51	84.21
+ GIQT	88.76	82.59	88.13	81.70	91.13	85.63	88.76	82.59
+ GCPG + GIQT	90.15	84.49	89.45	83.18	92.80	87.54	90.77	84.71
<i>Geometry Embedding Analysis</i>								
w/o Cam	90.32	84.71	89.84	83.54	93.30	87.80	90.94	84.55
w/o Alt	88.67	82.61	88.57	81.76	91.58	85.71	88.85	82.58
w/o Ang	90.15	84.38	89.84	83.65	92.76	87.83	90.43	84.86

TABLE VIII
ABLATION STUDY ON CARGO

Method	All		G→G		A→A		A→G	
	R1	mAP	R1	mAP	R1	mAP	R1	mAP
+ GCPG	70.83	63.94	86.61	80.79	85.00	69.08	71.28	68.41
+ GIQT	72.76	64.62	88.39	79.40	82.50	68.90	72.34	68.52
<i>Geometry Embedding Analysis</i>								
w/o Cam	69.87	63.29	85.71	80.31	82.50	69.55	67.02	65.23
w/o Alt	69.23	63.60	84.82	80.36	85.00	68.50	69.15	68.95
w/o Ang	69.87	63.97	86.61	81.35	80.00	66.74	69.15	67.73

A↔G Rank-1 accuracy from 87.02% to 84.50%, while removing camera identity results in a smaller drop. Similar trends are observed on AG-ReIDv2, CARGO, and DETReIDX. These results indicate that geometry cues altitude and viewing angle are the dominant factors governing geometry induced similarity distortion, while camera identity primarily provides coarse contextual bias.

E. Analysis of Design Choices

This subsection provides empirical justification for the architectural and modeling choices of the proposed framework. All analyses are conducted consistently across AG-ReID, AG-ReIDv2, CARGO, and DETReIDX, covering both metadata rich and metadata free settings, as well as moderate to extreme viewpoint disparity.

Structure of Geometry Induced Distortion

We first analyze the structure of cross view geometric distortion by examining the singular value spectrum of the covariance difference between aerial and ground features. As shown in Fig. 4, the spectrum exhibits pronounced decay, indicating that geometry induced distortion is highly anisotropic rather than uniformly distributed across feature dimensions. Notably, the top-8 singular components capture approximately 19.4% of the total energy, while the top-16 components capture 32.6%, far exceeding a uniform-energy baseline. This observation

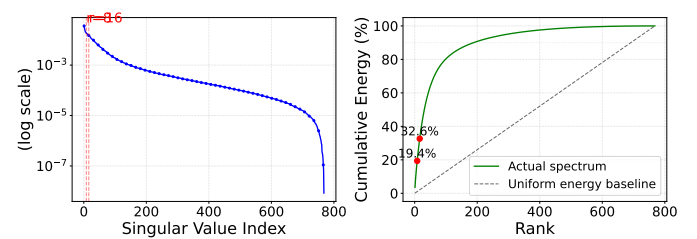


Fig. 4. Singular value spectrum and cumulative energy distribution of cross view feature covariance difference, showing highly anisotropic geometry induced distortion.

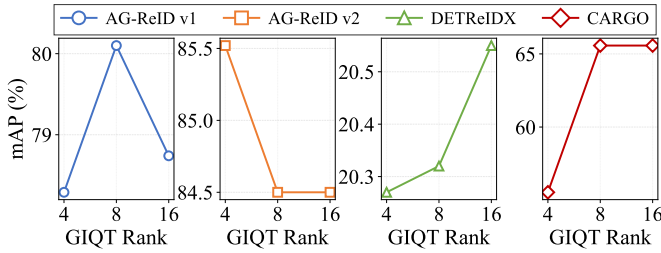


Fig. 5. Performance sensitivity with respect to GIQT rank across datasets. Low rank correction (8–16) yields optimal performance.

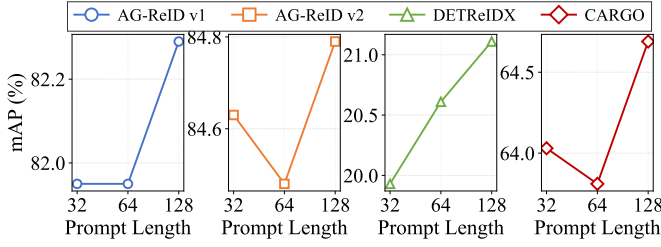


Fig. 6. Effect of geometry conditioned prompt length across datasets. Performance remains stable over a wide range of prompt sizes.

motivates the low rank residual formulation adopted in the GIQT, which targets dominant geometry sensitive directions without overfitting higher order variations.

Sensitivity to GIQT Rank

Figure 5 analyzes the effect of the GIQT rank on performance across AG-ReIDv1, AG-ReIDv2, DETReIDX, and CARGO. Across all datasets, performance improves when increasing the rank from 4 to 8 and either saturates or slightly degrades beyond rank 16. In particular, AG-ReIDv1 achieves its peak mAP at rank 8, while AG-ReIDv2 and CARGO exhibit marginal gains up to rank 16. DETReIDX, which features more severe geometric distortion, also benefits most from low-to-moderate ranks. These results indicate that geometry induced distortion is dominated by a small number of directions and that low-rank correction (8–16) is sufficient, while higher ranks provide diminishing returns and risk of overfitting.

Sensitivity to geometry conditioned prompt length

Figure 6 evaluates the impact of geometry conditioned prompt length. Performance remains stable across a wide range of prompt sizes (32–128 tokens) on all datasets. AG-ReIDv1 and AG-ReIDv2 show minor fluctuations, while DETReIDX and CARGO exhibit slightly better performance with longer prompts. These results demonstrate that the proposed GCPG mechanism is robust to prompt length and does not require careful tuning, indicating that geometry information is encoded compactly rather than relying on excessive prompt capacity.

Hidden Dimension Sensitivity Figure 7 analyzes the effect of increasing the hidden dimension across all four benchmarks. Across AG-ReID, AG-ReIDv2, CARGO, and DETReIDX, increasing the hidden dimension beyond 512 does not yield consistent improvements and in several cases slightly degrades performance. This behavior indicates that cross view performance degradation under extreme aerial-ground geometry is

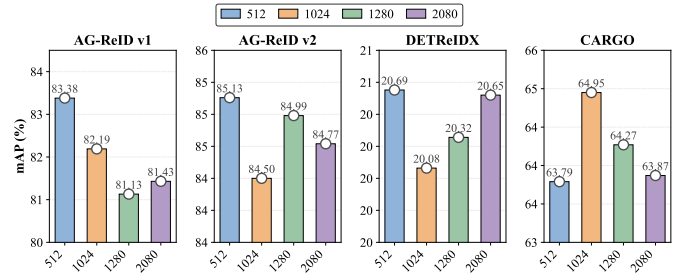


Fig. 7. Effect of hidden dimension size across datasets. Increasing feature dimensionality beyond 512 does not yield consistent gains, indicating that geometry induced similarity distortion—not model capacity is the dominant bottleneck.

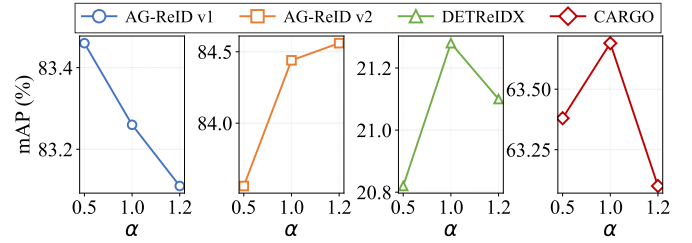


Fig. 8. Sensitivity to geometry-conditioned prompt scaling factor α across datasets. Performance peaks near $\alpha = 1.0$, indicating that geometry prompts should bias representations rather than dominate identity features.

not caused by insufficient representational capacity. Simply increasing feature dimensionality does not resolve the dominant failure mode. Instead, the limiting factor lies in the mismatch of the similarity space induced by geometric distortion. This observation provides further justification for explicitly rectifying similarity computation via geometry conditioned query-key transformation, rather than increasing model capacity or relying on wider embeddings.

Sensitivity to Prompt Scaling Figure 8 analyses the effect of the geometry-conditioned prompt scaling factor α across all four benchmarks. Across datasets, performance consistently peaks around $\alpha = 1.0$ and degrades when the prompt contribution is either underscaled or over-emphasised. When α is too small, geometry-conditioned prompts fail to provide sufficient bias to compensate for viewpoint-induced distortion. Conversely, when α is too large, geometry cues begin to dominate identity-discriminative features, leading to reduced retrieval performance. This behaviour is particularly evident on CARGO and DETReIDX, where extreme viewpoint disparity and noisy geometry estimation amplify the negative effects of over-scaling. These results confirm that geometry-conditioned prompts should act as a structured bias rather than a dominant representation component. The residual prompt formulation enables controlled adaptation, allowing geometry information to guide feature extraction without overwhelming identity semantics.

Corruption definitions.

Random bin flip (Altitude / Angle) randomly shifts the corresponding geometry bin by ± 1 , clipped to valid bin boundaries. *Joint bin perturbation* applies independent ± 1 shifts to both altitude and angle bins. *Biased altitude shift* applies a

TABLE IX

ROBUSTNESS TO DISCRETIZED GEOMETRY METADATA CORRUPTION ACROSS DATASETS. RESULTS ARE REPORTED UNDER PROTOCOL 1 ($A \leftrightarrow G$) FOR AG-ReID AND $A \rightarrow G$ FOR DETReIDX. AG-ReID USES 3 ALTITUDE BINS AND 3 VIEWING-ANGLE BINS, WHILE DETReIDX USES 6 ALTITUDE BINS AND 3 VIEWING-ANGLE BINS. ALL CORRUPTIONS ARE APPLIED *only at inference time* TO GEOMETRY INPUTS, USING MODELS TRAINED WITH CLEAN GEOMETRY. $\Delta R1$ (BASELINE) IS COMPUTED RELATIVE TO THE GEOMETRY-AGNOSTIC SECAP BASELINE (84.03% RANK-1 FOR AG-ReID AND 17.05% RANK-1 FOR DETReIDX).

Corruption Type	AG-ReID		DetReIDX	
	Rank-1	$\Delta R1$ (Base)	Rank-1	$\Delta R1$ (Base)
Clean geometry	87.02	+2.99	20.84	+3.79
Random bin flip (Altitude)	86.12	+2.09	20.12	+3.07
Random bin flip (Angle)	85.71	+1.68	19.63	+2.58
Joint bin perturbation	84.98	+0.95	19.05	+2.00
Biased altitude shift	84.61	+0.58	18.67	+1.62
Stale geometry	85.23	+1.20	19.34	+2.29
Wrong geometry	84.17	+0.14	18.21	+1.16

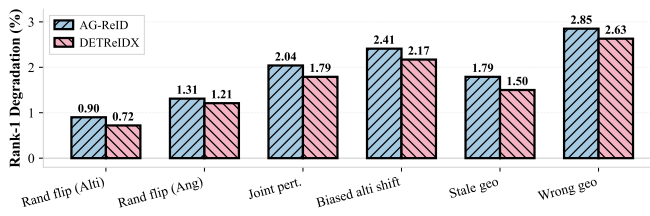


Fig. 9. Robustness to discretized geometry metadata corruption. The y-axis shows Rank-1 degradation relative to clean geometry. All corruptions are applied only at inference time using models trained with clean geometry. Results are reported for AG-ReID ($A \leftrightarrow G$) and DetReIDX ($A \rightarrow G$).

fixed +1 altitude-bin offset to all samples. *Stale geometry* assigns geometry bins from a temporally adjacent or nearby sample, simulating delayed or asynchronous metadata. *Wrong geometry* randomly shuffles geometry bins across identities, breaking geometry–image correspondence while preserving the marginal bin distribution. All perturbations are applied independently per image and consistently to both query and gallery samples.

F. Visualization Analysis

Qualitative Retrieval Analysis

Figure 10 presents representative Rank-1 to Rank-5 retrieval results comparing the baseline (SeCap) and the proposed method under challenging aerial–ground matching scenarios. Correct matches are highlighted in green, while incorrect matches are shown in red. The baseline frequently retrieves visually similar but incorrect identities under extreme viewpoint changes, particularly when aerial queries induce strong foreshortening, scale compression, or body-part displacement. In these cases, similarity scores are dominated by spurious local alignments, leading to incorrect high-rank matches despite overall appearance resemblance. In contrast, the proposed method consistently retrieves correct identities at higher ranks. Notably, improvements are observed not only at Rank-1 but also across the entire top- k list, indicating more reliable similarity ordering rather than isolated corrections. This behavior suggests that geometry-induced distortion in the



Fig. 10. Qualitative comparison of Rank-1 to Rank-5 retrieval results between the baseline (SeCap) and the proposed method. The baseline suffers from incorrect high-rank matches due to geometry-induced similarity distortion, while the proposed method produces more consistent and correct ranking under extreme aerial–ground viewpoint differences.

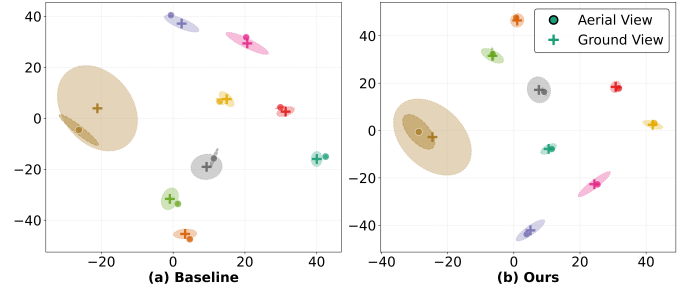


Fig. 11. 2D t-SNE visualization of aerial and ground view feature embeddings for the baseline and our proposed method. Circles (●) represent the geometric mean aerial-view samples, and plus symbols (+) represent ground-view samples, while the shaded areas provide the ellipses that contain 90% of the corresponding data points. Colors indicate identity labels.

similarity space is explicitly mitigated, enabling more consistent alignment of corresponding body regions across views. These qualitative results complement the quantitative gains, illustrating that geometry-conditioned similarity rectification improves ranking stability under extreme cross-view viewpoint discrepancies.

G. Feature Space Visualization

Figure 11 provides the learned feature distributions of the baseline model and the proposed method using t-SNE. Each color denotes a identity, while circles and crosses represent aerial and ground views, respectively. In the baseline model, features corresponding to the same identity but different views exhibit noticeable separation and overlap with other identities. This indicates that although identity-level clustering exists, cross-view alignment remains inconsistent, leading to fragmented clusters and view-dependent feature drift. In contrast,

the proposed method produces more compact and well-aligned clusters across views. Features from aerial and ground cameras corresponding to the same identity are more tightly grouped, while inter-identity separation is preserved. Importantly, this improvement is not achieved by collapsing representations, but by reducing cross-view dispersion within each identity cluster. While t-SNE is a qualitative visualization tool, the observed reduction in cross-view overlap and improved cluster compactness are consistent with the quantitative gains reported earlier. These results suggest that geometry-conditioned prompt adaptation and similarity-space rectification jointly encourage more view-consistent representations.

V. CONCLUSION

This work identified the *geometry-induced distortion in the similarity space* factor as a key failure mode in aerial-ground person re-identification. As a consequence, we concluded that the geometry-invariant similarity assumption underlying attention does not hold, even when feature representations are partially aligned. To address this issue, we introduced a geometry-conditioned similarity alignment framework that explicitly incorporates camera geometry into both global representation adaptation and local similarity computation. The proposed Geometry-Induced Query-Key Transformation (GIQT) rectifies dominant, anisotropic similarity distortions through a lightweight low-rank formulation, while geometry-conditioned prompts provide complementary global adaptation. Extensive experiments across four benchmarks suggest that explicitly correcting the similarity space consistently improves robustness under extreme, corrupted, and unseen geometric conditions, with minimal computational overhead. These findings highlight the importance of geometry-aware similarity modeling for reliable cross-view recognition in *real-world* aerial-ground scenarios.

ACKNOWLEDGEMENTS

This work is funded by national funds through FCT – Fundação para a Ciência e a Tecnologia, I.P., and, when eligible, co-funded by EU funds under project/support UID/50008/2025 – Instituto de Telecomunicações, with DOI identifier <https://doi.org/10.54499/UID/50008/2025>.

REFERENCES

- [1] S. Zhang, Q. Yang, D. Cheng, Y. Xing, G. Liang, P. Wang, and Y. Zhang, “Ground-to-Aerial Person Search: Benchmark Dataset and Approach,” *Proceedings of the 31st ACM International Conference on Multimedia*, pp. 789–799, 2023.
- [2] Y.-C. Chen, X. Zhu, W.-S. Zheng, and J.-H. Lai, “Person re-identification by camera correlation aware feature augmentation,” *IEEE Transactions on Pattern Analysis and Machine Intelligence*, vol. 40, no. 2, pp. 392–408, Feb. 2018.
- [3] L. Zheng, Y. Yang, and A. G. Hauptmann, “Person re-identification: Past, present and future,” *arXiv:1610.02984*, 2016.
- [4] X. Liu, W. Liu, H. Ma, and H. Fu, “Large-scale vehicle re-identification in urban surveillance videos,” in *Proc. IEEE Int. Conf. Multimedia Expo (ICME)*, Jul. 2016, pp. 1–6.
- [5] X. Liu, W. Liu, T. Mei, and H. Ma, “A deep learning-based approach to progressive vehicle re-identification for urban surveillance,” in *Proc. Eur. Conf. Comput. Vis. (ECCV)*, 2016, pp. 869–884.
- [6] H. Li, M. Ye, C. Wang, and B. Du, “Pyramidal transformer with conv-patchify for person re-identification,” in *Proc. ACM international conference Multimedia (ACM MM)*, 2022, pp. 7317–7326.
- [7] S. Yang, B. Kang, and Y. Lee, “Sampling agnostic feature representation for long-term person re-identification,” *IEEE Transactions on Image Processing*, vol. 31, pp. 6412–6423, 2022.
- [8] G. Chen, T. Gu, J. Lu, J.-A. Bao, and J. Zhou, “Person re-identification via attention pyramid,” *IEEE Transactions on Image Processing*, vol. 30, pp. 7663–7676, 2021.
- [9] X. Tian, J. Liu, Z. Zhang, C. Wang, Y. Qu, Y. Xie, and L. Ma, “Hierarchical walking transformer for object re-identification,” in *Proceedings of the 30th ACM International Conference on Multimedia*, 2022, pp. 4224–4232.
- [10] S. Zhang, Q. Zhang, Y. Yang, X. Wei, P. Wang, B. Jiao, and Y. Zhang, “Person re-identification in aerial imagery,” *IEEE Transactions on Multimedia*, vol. 23, pp. 281–291, 2020.
- [11] T. Li, J. Liu, W. Zhang, Y. Ni, W. Wang, and Z. Li, “UAV-Human: A large benchmark for human behavior understanding with unmanned aerial vehicles,” in *Proceedings of the IEEE/CVF Conference on Computer Vision and Pattern Recognition*, 2021, pp. 16266–16275.
- [12] P. Wang, B. Jiao, L. Yang, Y. Yang, S. Zhang, W. Wei, and Y. Zhang, “Vehicle re-identification in aerial imagery: Dataset and approach,” in *Proceedings of the IEEE/CVF International Conference on Computer Vision*, 2019, pp. 460–469.
- [13] S. V. A. Kumar, E. Yaghoubi, A. Das, B. S. Harish, and H. Proença, “The P-DESTRE: A fully annotated dataset for pedestrian detection, tracking, and short/long-term re-identification from aerial devices,” *IEEE Transactions on Information Forensics and Security*, vol. 16, pp. 1696–1708, 2020.
- [14] S. Teng, S. Zhang, Q. Huang, and N. Sebe, “Viewpoint and scale consistency reinforcement for UAV vehicle re-identification,” *International Journal of Computer Vision*, vol. 129, no. 3, pp. 719–735, 2021.
- [15] S. He, H. Luo, P. Wang, F. Wang, H. Li, and W. Jiang, “TransReID: Transformer-based object re-identification,” in *Proceedings of the IEEE/CVF International Conference on Computer Vision*, 2021, pp. 15013–15022.
- [16] W. Li, C. Zou, M. Wang, F. Xu, J. Zhao, R. Zheng, Y. Cheng, and W. Chu, “DC-Former: Diverse and compact transformer for person re-identification,” in *Proceedings of the AAAI Conference on Artificial Intelligence*, vol. 37, no. 2, 2023, pp. 1415–1423.
- [17] L. Tan, P. Dai, J. Chen, L. Cao, Y. Wu, and R. Ji, “PartFormer: Awakening latent diverse representation from vision transformer for object re-identification,” *arXiv preprint arXiv:2408.16684*, 2024.
- [18] G. Zhang, Y. Zhang, T. Zhang, B. Li, and S. Pu, “PHA: Patch-wise high-frequency augmentation for transformer-based person re-identification,” in *Proceedings of the IEEE/CVF Conference on Computer Vision and Pattern Recognition*, 2023, pp. 14133–14142.
- [19] S. Li, L. Sun, and Q. Li, “CLIP-ReID: Exploiting vision-language model for image re-identification without concrete text labels,” in *Proceedings of the AAAI Conference on Artificial Intelligence*, vol. 37, no. 1, 2023, pp. 1405–1413.
- [20] L. Tan, Y. Zhang, K. Han, P. Dai, Y. Zhang, Y. Wu, and R. Ji, “RLE: A unified perspective of data augmentation for cross-spectral re-identification,” *Advances in Neural Information Processing Systems*, vol. 37, pp. 126977–126996, 2024.
- [21] Y. Li, J. He, T. Zhang, X. Liu, Y. Zhang, and F. Wu, “Diverse part discovery: Occluded person re-identification with part-aware transformer,” in *Proceedings of the IEEE/CVF Conference on Computer Vision and Pattern Recognition*, 2021, pp. 2898–2907.
- [22] C. Wang, Y. Yang, M. Qi, H. Zhang, and H. Ma, “Towards Efficient Object Re-Identification with a Novel Cloud-Edge Collaborative Framework,” in *Proceedings of the AAAI Conference on Artificial Intelligence*, vol. 39, no. 7, 2025, pp. 7600–7608.
- [23] Y. Feng, J. Li, C. Xie, L. Tan, and J. Ji, “Multi-Modal Object Re-identification via Sparse Mixture-of-Experts,” in *Proceedings of the Forty-Second International Conference on Machine Learning*.
- [24] Y. Jia, R. Quan, Y. Feng, H. Chen, and J. Qin, “Doubly Contrastive Learning for Source-Free Domain Adaptive Person Search,” in *Proceedings of the AAAI Conference on Artificial Intelligence*, vol. 39, no. 4, 2025, pp. 3949–3957.
- [25] H. Nguyen, K. Nguyen, S. Sridharan, and C. Fookes, “Aerial-ground person re-ID,” in *2023 IEEE International Conference on Multimedia and Expo (ICME)*, 2023, pp. 2585–2590.
- [26] H. Nguyen, K. Nguyen, S. Sridharan, and C. Fookes, “AG-ReID.v2: Bridging aerial and ground views for person re-identification,” *IEEE Transactions on Information Forensics and Security*, vol. 19, pp. 2896–2908, 2024.
- [27] Q. Zhang, L. Wang, V. M. Patel, X. Xie, and J. Lai, “View-decoupled transformer for person re-identification under aerial-ground camera

network,” in *Proceedings of the IEEE/CVF Conference on Computer Vision and Pattern Recognition*, 2024, pp. 22000–22009.

[28] K. A. Hambarde, N. Mbongo, P. K. MP, S. Mekewad, C. Fernandes, G. Silahtaroğlu, A. Nithya, P. Wasnik, M. D. Rashidunnabi, P. Samale, *et al.*, “DetReIDX: A stress-test dataset for real-world UAV-based person recognition,” *arXiv preprint arXiv:2505.04793*, 2025.

[29] F. Liu, L. Yao, C. Zhang, T. Wu, X. Zhang, X. Jiang, and J. Zhou, “Boost UAV-based object detection via scale-invariant feature disentanglement and adversarial learning,” *IEEE Transactions on Geoscience and Remote Sensing*, 2025.

[30] C. Yan, G. Pang, L. Wang, J. Jiao, X. Feng, C. Shen, and J. Li, “BV-Person: A large-scale dataset for bird-view person re-identification,” in *Proceedings of the IEEE/CVF International Conference on Computer Vision*, 2021, pp. 10943–10952.

[31] S. Wang, Y. Wang, R. Wu, B. Jiao, W. Wang, and P. Wang, “Se-Cap: Self-Calibrating and Adaptive Prompts for Cross-view Person Re-Identification in Aerial-Ground Networks,” in *Proceedings of the Computer Vision and Pattern Recognition Conference*, 2025, pp. 22119–22128.

[32] Z. Liu, Y. Lin, Y. Cao, H. Hu, Y. Wei, Z. Zhang, S. Lin, and B. Guo, “Swin Transformer: Hierarchical vision transformer using shifted windows,” in *Proceedings of the IEEE/CVF International Conference on Computer Vision*, 2021, pp. 10012–10022.

[33] K. Hambarde and H. Proenca, “Image-based human re-identification: Which covariates are actually (the most) important?” *Image and Vision Computing*, vol. 143, p. 104917, 2024.

[34] S. Zhang, W. Luo, D. Cheng, Q. Yang, L. Ran, Y. Xing, and Y. Zhang, “Cross-platform video person re-identification: A new benchmark dataset and adaptation approach,” in *Proceedings of the European Conference on Computer Vision (ECCV)*, 2024, pp. 270–287.

[35] K. Nguyen, F. Liu, C. Fookes, S. Sridharan, X. Liu, and A. Ross, “Person Recognition in Aerial Surveillance: A Decade Survey,” *IEEE Transactions on Biometrics, Behavior, and Identity Science*, 2025.

[36] W. Khalid, B. Liu, X. Li, M. Waqas, and M. S. Afgan, “Bridging the Sky and Ground: Towards View-Invariant Feature Learning for Aerial-Ground Person Re-Identification,” in *Proceedings of the IEEE/CVF International Conference on Computer Vision (ICCV)*, 2025, pp. 9749–9758.

[37] Y. Wang, X. Hu, L. Wang, P. Zhang, and H. Lu, “SD-ReID: View-aware Stable Diffusion for Aerial-Ground Person Re-Identification,” *arXiv preprint arXiv:2504.09549*, 2025.

[38] L. Wang, Q. Zhang, J. Qiu, and J. Lai, “Rotation Exploration Transformer for Aerial Person Re-Identification,” in *Proceedings of the IEEE International Conference on Multimedia and Expo (ICME)*, 2024, pp. 1–6.

[39] F. Zhang, E. Firkat, H. Ma, J. Zhu, B. Zhu, and A. Hamdulla, “DARI: Transformer-Based Data Augmentation and Rotation Invariance for UAV Person Re-Identification,” *IEEE Transactions on Multimedia*, 2025.

[40] S. Chen, M. Ye, Y. Huang, and B. Du, “Towards Effective Rotation Generalization in UAV Object Re-Identification,” *IEEE Transactions on Information Forensics and Security*, 2025.

[41] Q. Li, J. Li, Y. Zhang, L. Tan, J. Chen, and J. Ji, “GSAlign: Geometric and Semantic Alignment Network for Aerial-Ground Person Re-Identification,” *arXiv preprint arXiv:2510.22268*, 2025.

[42] J. Qiu, Z. Feng, L. Wang, and J. Lai, “Salient Part-Aligned and Keypoint Disentangling Transformer for Person Re-Identification in Aerial Imagery,” in *Proceedings of the IEEE International Conference on Multimedia and Expo (ICME)*, 2024, pp. 1–6.

[43] Y. Wang and M. Pishgar, “Dynamic Token Selection for Aerial-Ground Person Re-Identification,” *arXiv preprint arXiv:2412.00433*, 2024.

[44] Y. Wang, M. Yang, R. Cao, and G. Gao, “AEA-FIRM: Adaptive Elastic Alignment with Fine-Grained Representation Mining for Text-based Aerial Pedestrian Retrieval,” *IEEE Transactions on Circuits and Systems for Video Technology*, 2025.

[45] P. Zhang, X. Hu, Y. Wang, and H. Lu, “Latex: Leveraging Attribute-Based Text Knowledge for Aerial-Ground Person Re-Identification,” *arXiv preprint arXiv:2503.23722*, 2025.

[46] J. Li, Z. Chen, L. Deng, C. Wang, and G. Zhai, “MMReID-Bench: Unleashing the Power of MLLMs for Effective and Versatile Person Re-Identification,” *arXiv e-prints*, arXiv:2508, 2025.

[47] L. He, X. Liao, W. Liu, X. Liu, P. Cheng, and T. Mei, “FastReID: A PyTorch Toolbox for General Instance Re-Identification,” in *Proceedings of the 31st ACM International Conference on Multimedia (ACM MM)*, 2023, pp. 9664–9667.

[48] H. Luo, Y. Gu, X. Liao, S. Lai, and W. Jiang, “Bag of Tricks and a Strong Baseline for Deep Person Re-Identification,” in *Proceedings of the IEEE/CVF Conference on Computer Vision and Pattern Recognition Workshops (CVPRW)*, Jun. 2019, pp. 1487–1495.

[49] K. Zhou, Y. Yang, A. Cavallaro, and T. Xiang, “Learning Generalisable Omni-Scale Representations for Person Re-Identification,” *IEEE Transactions on Pattern Analysis and Machine Intelligence*, vol. 44, no. 9, pp. 5056–5069, 2021.

[50] R. Kuma, E. Weill, F. Aghdasi, and P. Sriram, “Vehicle Re-Identification: An Efficient Baseline Using Triplet Embedding,” in *2019 International Joint Conference on Neural Networks (IJCNN)*, 2019, pp. 1–9.

[51] A. Dosovitskiy, “An Image is Worth 16x16 Words: Transformers for Image Recognition at Scale,” *arXiv preprint arXiv:2010.11929*, 2020.

[52] J. Wang, K. Sun, T. Cheng, B. Jiang, C. Deng, Y. Zhao, D. Liu, Y. Mu, M. Tan, X. Wang, *et al.*, “Deep high-resolution representation learning for visual recognition,” *IEEE Transactions on Pattern Analysis and Machine Intelligence*, vol. 43, no. 10, pp. 3349–3364, 2020.

[53] Z. Liu, H. Hu, Y. Lin, Z. Yao, Z. Xie, Y. Wei, J. Ning, Y. Cao, Z. Zhang, L. Dong, *et al.*, “Swin Transformer V2: Scaling up capacity and resolution,” in *Proceedings of the IEEE/CVF Conference on Computer Vision and Pattern Recognition (CVPR)*, pp. 12009–12019, 2022.

[54] G. Wang, Y. Yuan, X. Chen, J. Li, and X. Zhou, “Learning discriminative features with multiple granularities for person re-identification,” in *Proceedings of the 26th ACM International Conference on Multimedia (ACM MM)*, pp. 274–282, 2018.

[55] K. Nguyen, C. Fookes, S. Sridharan, F. Liu, X. Liu, A. Ross, D. Michalski, H. Nguyen, D. Deb, M. Kothari, *et al.*, “AG-ReID 2023: Aerial-ground person re-identification challenge results,” in *2023 IEEE International Joint Conference on Biometrics (IJCB)*, pp. 1–10, 2023.

[56] Y. Wang, P. Zhang, X. Liu, Z. Tu, and H. Lu, “Unity is strength: Unifying convolutional and transformer features for better person re-identification,” *IEEE Transactions on Intelligent Transportation Systems*, 2025.

[57] J. Li and X. Gong, “Prototypical contrastive learning-based CLIP finetuning for object re-identification,” *arXiv preprint arXiv:2310.17218*, 2023.

[58] D. Mao, S. Teng, and X. Lv, “CVAF: A CLIP-Based View-Consistent Alignment Framework for Aerial-Ground Person Re-Identification,” *ACM Transactions on Multimedia Computing, Communications and Applications*, 2025.

[59] T. Wang, H. Liu, P. Song, T. Guo, and W. Shi, “Pose-guided feature disentangling for occluded person re-identification based on transformer,” in *Proceedings of the AAAI Conference on Artificial Intelligence*, vol. 36, no. 3, pp. 2540–2549, 2022.

[60] M. Ye, J. Shen, G. Lin, T. Xiang, L. Shao, and S. C. Hoi, “Deep learning for person re-identification: A survey and outlook,” *IEEE Transactions on Pattern Analysis and Machine Intelligence*, vol. 44, no. 6, pp. 2872–2893, 2021.

[61] Y. Cho, J. Kim, W. J. Kim, J. Jung, and S.-E. Yoon, “Generalizable person re-identification via balancing alignment and uniformity,” *Advances in Neural Information Processing Systems*, vol. 37, pp. 47069–47093, 2024.

[62] H. Ni, Y. Li, L. Gao, H. T. Shen, and J. Song, “Part-aware transformer for generalizable person re-identification,” in *Proceedings of the IEEE/CVF International Conference on Computer Vision (ICCV)*, pp. 11280–11289, 2023.

[63] Y. Sun, L. Zheng, Y. Li, Y. Yang, Q. Tian, and S. Wang, “Learning part-based convolutional features for person re-identification,” *IEEE Transactions on Pattern Analysis and Machine Intelligence*, vol. 43, no. 3, pp. 902–917, 2019.

[64] H. Moon and P. J. Phillips, “Computational and performance aspects of PCA-based face-recognition algorithms,” *Perception*, vol. 30, no. 3, pp. 303–321, 2001.

[65] L. Zheng, L. Shen, L. Tian, S. Wang, J. Wang, and Q. Tian, “Scalable person re-identification: A benchmark,” in *Proceedings of the IEEE International Conference on Computer Vision (ICCV)*, 2015, pp. 1116–1124.

[66] L. Bottou, “Large-scale machine learning with stochastic gradient descent,” in *Proceedings of the 19th International Conference on Computational Statistics (COMPSTAT)*, 2010, pp. 177–186.

[67] Z. Zhong, L. Zheng, G. Kang, S. Li, and Y. Yang, “Random erasing data augmentation,” in *Proceedings of the AAAI Conference on Artificial Intelligence*, vol. 34, no. 7, 2020, pp. 13001–13008.